

Application of temporal filters to time resolved data in optical tomography

Martin Schweiger† and Simon R Arridge‡

† Department of Medical Physics and Bioengineering, University College London,
11-20 Capper Street, London WC1E 6JA, UK

‡ Department of Computer Science, University College London, Gower Street,
London WC1E 6BT, UK

Received 22 December 1998, in final form 29 March 1999

Abstract. This paper addresses the problem of selecting measurement data types suitable for image reconstruction in optical tomography. The principal problem is the necessity to simultaneously reconstruct both the absorption and scatter distribution within an object. This can lead to ambiguities between these two parameters, and result in cross-talk and image artefact.

A single-perturbation test problem is used to show that the ability to separate the absorption and scatter maps depends critically on the measurement data types used in the reconstruction, and that significant improvement can be achieved by a combination of suitable data sets.

These results are verified by performing reconstructions of a simulated test object with a complex internal structure of embedded inhomogeneities, from which a variety of time-domain forward data sets are calculated. It is shown that dc data are insufficient to separate absorption and scatter features in the images, whereas a combination of moments and Laplace transforms of the temporal measurement signal provides the best reconstruction results of the data types investigated.

1. Introduction

Near-infrared imaging, or optical tomography (OT), is potentially a powerful tool to non-invasively obtain spatially resolved data of the optical parameters of tissue, from which physiologically relevant information such as local oxygenation levels can be calculated. Primary applications of this new imaging modality are the monitoring of cerebral blood and tissue oxygenation of newborn and preterm infants (Edwards *et al* 1988, Wyatt *et al* 1990) to prevent death or permanent brain damage caused by asphyxiation during birth, functional mapping of brain activation during physical or mental exercise (Ntzachristos *et al* 1999), and imaging of the breast to detect tumours (Hebden *et al* 1991).

Light transport in biological tissue in the near-infrared wavelength range is dominated by scattering, and the unscattered component at a penetration depth of several centimetres is negligible. Scatter causes light to propagate diffusely in tissue and restricts the application of direct reconstruction methods using the Radon transform. To reduce the influence of light scattering, some authors have suggested the use of time-gating techniques, whereby only the first arriving photons contribute to the measurement; these photons have undergone only a few scattering events and have not deviated significantly from the straight line path, thus reducing the image reconstruction to a Radon transform approximation. Due to loss in signal-to-noise ratio, however, this technique is restricted to very small optical thicknesses and is not generally applicable.

Various reconstruction methods, including backprojection schemes (Colak *et al* 1996, Walker *et al* 1996), and semi-analytic schemes (O’Leary *et al* 1995) have been proposed, but due to the nonlinearity of the problem, iterative, optimization-based schemes are increasingly employed (Arridge *et al* 1992, Jiang *et al* 1995, Pogue *et al* 1995). Our iterative approach uses a finite-element model to solve the diffusion forward problem, and has a choice of optimization algorithms to solve the inverse problem. The method has been reported previously (Arridge *et al* 1993a, Schweiger *et al* 1993), and is briefly outlined in sections 3 and 4 below. Recent review articles include works by Hebden *et al* (1997) and Arridge and Hebden (1997).

A key factor in optical tomography is the presence of two parameters, absorption and scattering. Although absorption is the image of primary interest, the presence of unknown scatter can lead to artefacts and false structure in the reconstructions. It is necessary either to assume that scatter is constant and known, or to include it in the image reconstruction process. This situation can be compared with SPECT (single photon emission computed tomography), where the two parameters are activity and attenuation. Failure to adequately account for the latter leads to artefacts (Bronnikov 1995, Censor *et al* 1979). In optical tomography it is known that for the dc case, for any change in absorption between two states giving rise to a change in data, there also exists an equivalent scatter distribution giving rise to the same change (Arridge and Lionheart 1998). In theory either frequency domain or time domain measurements allow the reconstruction of two parameters. O’Leary *et al* (1995) showed reconstruction of absorption and scatter with some ‘cross-talk’ between the two. Jiang *et al* (1998) showed that quantitative reconstructions could be obtained for the particular case where the μ_a and μ_s images had the same relative cross section.

In the approach taken by our group, we employ time-resolved measurements because of the potentially greater information content available. In this paper we investigate the degree to which choice of information derived from time-resolved data affects the particular problem of separation of reconstructions in absorption and scatter images. In section 2 we discuss data type choices and in sections 3 and 4 briefly review the forward and inverse models used in this paper. In section 5 we present a study of the error surface from a simple two-dimensional problem to illustrate the effect of data choice on nonlinearity and ill-posedness of the inverse problem. In section 6 we present simulated reconstructions from different data types and propose the choice of two data types that are optimal for reducing cross-talk artefacts.

The aim of this paper is to demonstrate that the choice of data types can profoundly affect the ability to simultaneously reconstruct both parameters. We have limited the problems discussed here to two-dimensional test cases, to reduce the computational complexity. The findings of section 5 still hold in three-dimensional problems. In addition, the two-dimensional reconstructions in section 6 are valid in their own right because we have recently shown that for certain problems data obtained on a three-dimensional object can be used successfully in two-dimensional reconstructions (Schweiger and Arridge 1998).

2. Measurement data types in the time domain

The aim in OT is to reconstruct the spatial distribution of the optical parameters of a volume of tissue from a set of boundary measurements on the tissue surface. Let Ω be the domain under consideration, with surface $\partial\Omega$. We consider s source positions $\zeta_i \in \partial\Omega$ ($i = 1 \dots s$) and m_i measurement positions $\xi_j \in \partial\Omega$ for each source i ($j = 1 \dots m_i$), resulting in a total number of measurements $n = \sum_{i=1}^s m_i$. For each source i the response signal at all measurement sites j is recorded. The type of measurement depends on the data acquisition system employed. In dc systems, the measurement is the steady-state attenuation between source and detector locations. Time-of-flight systems using an ultra-short pulsed laser as a light source and time-resolved

detectors allow the boundary measurement of the temporal intensity response function with a resolution of a few picoseconds (Delpy *et al* 1988). Frequency domain systems use a radio-frequency modulated light source and measure the phaseshift and modulation amplitude of the transmitted light (Chance *et al* 1990). Data from all three types of data acquisition systems has been used in image reconstruction (Jiang *et al* 1995, 1996, Arridge and Schweiger 1995a).

In time-domain systems, the measurement is the temporally resolved boundary current, or *exitance* $\Gamma_i(\xi_j, t)$ at detector position ξ_j , caused by a source pulse at ζ_i . While it is possible to use the full temporal profile, sampled at discrete time steps, as the data vector passes to the inverse solver (Cai *et al* 1996), we consider as data types y the following integral transforms of Γ . The motive for using these temporal filters is to reduce the redundancy in the data set, given the fact that the temporal profiles exhibit no high-frequency features (Delpy *et al* 1998).

$$\text{integrated intensity: } y_{ij} = E = \int_0^{\infty} \Gamma_i(\xi_j, t) dt \quad (1)$$

$$n\text{-th temporal moment: } y_{ij} = \langle t^n \rangle = E^{-1} \int_0^{\infty} t^n \Gamma_i(\xi_j, t) dt \quad (2)$$

$$n\text{-th central moment: } y_{ij} = c_n = E^{-1} \int_0^{\infty} (t - \langle t \rangle)^n \Gamma_i(\xi_j, t) dt \quad (3)$$

$$\text{normalized Laplace transform: } y_{ij} = L(s) = E^{-1} \int_0^{\infty} e^{-st} \Gamma_i(\xi_j, t) dt \quad (4)$$

$$\text{Mellin-Laplace: } y_{ij} = ML_n(s) = E^{-1} \int_0^{\infty} t^n e^{-st} \Gamma_i(\xi_j, t) dt. \quad (5)$$

This list could be further extended. One could use for example the integral of Γ over a limited temporal period (time-gating), the logarithmic slope of the temporal decay of Γ , the peak intensity, etc. From this collection it will be apparent that time-domain OT systems provide a feature-rich environment for image reconstruction. With the availability of a large number of data types, the problem at hand is to select a combination of data sets which contains sufficient information to enable the simultaneous reconstruction of absorption and scatter distributions. The data types used in OT should meet the following conditions:

- (a) Robustness of measurement. A data type should be measurable with high signal-to-noise ratio and should not produce systematic errors due to fluctuations of the source power, detector sensitivity or fibre coupling losses.
- (b) Efficiency of forward modelling. Nonlinear iterative image reconstruction requires multiple evaluations of the selected data types by a forward model. Data types which can be modelled efficiently are therefore essential.
- (c) Maximization of information content. Highly correlated data types add little extra information but increase the computational cost of image reconstruction.

Data types (1) to (5) can all be calculated directly by our forward model without the need of explicitly generating the temporal profile of Γ (Arridge and Schweiger 1995b, Schweiger and Arridge 1997). In addition, all except the intensity (E) are normalized and therefore do not require knowledge of the absolute magnitude of Γ , which makes them robust against variations in source power or surface effects at the source or detector sites.

3. Forward model

Our approach has been to use the diffusion approximation to the radiative transfer equation, which in time domain is given by

$$\frac{\partial \Phi(\mathbf{r}, t)}{\partial t} - \nabla \cdot c(\mathbf{r})\kappa(\mathbf{r})\nabla \Phi(\mathbf{r}, t) + c(\mathbf{r})\mu_a(\mathbf{r})\Phi(\mathbf{r}, t) = q_0(\mathbf{r}, t) \quad (6)$$

where Φ is the isotropic photon density, q_0 is an isotropic source distribution and $c(\mathbf{r})$ is the speed of light in the medium. The model is characterized by the spatially varying absorption and diffusion coefficients, $\mu_a(\mathbf{r})$ and $\kappa(\mathbf{r})$, where

$$\kappa(\mathbf{r}) = \{3[\mu_a(\mathbf{r}) + \mu_s(\mathbf{r})]\}^{-1} \quad (7)$$

and $\mu_s(\mathbf{r})$ is the reduced or transport scattering coefficient. The third model parameter, refractive index $\nu(\mathbf{r}) = c_0/c(\mathbf{r})$, where $c_0 = 0.3 \text{ mm ps}^{-1}$ is the speed of light in a vacuum, is generally assumed to be known.

Diffusion theory assumes $\mu_a \ll \mu_s$ and only weakly anisotropic light propagation. While the former is generally true for biological tissues, the latter is violated near sources and boundaries. However, comparisons of diffusion calculations with experimental results (Madsen *et al* 1996, Fishkin and Gratton 1993) and Monte Carlo simulations (Farrell and Patterson 1992) show that diffusion models provide sufficient accuracy for most applications. Higher precision can be obtained, if required, by using higher-order approximations to the transfer equations, at the expense of increased computational effort in the implementation of the model.

The boundary measurement $\Gamma(\xi, t)$ at $\xi \in \partial\Omega$ is related to $\Phi(\mathbf{r}, t)$ by

$$\Gamma(\xi, t) = -c\kappa(\xi)\hat{n} \cdot \nabla \Phi(\xi, t) \quad (8)$$

where \hat{n} is the outer normal of $\partial\Omega$ at ξ . We use the Robin-type boundary condition

$$\Phi(\xi, t) + 2\kappa A\hat{n} \cdot \nabla \Phi(\xi, t) = 0 \quad (9)$$

where A is a term to incorporate boundary reflections as a result of a refractive index mismatch at $\partial\Omega$ (Schweiger *et al* 1995). Given a solution Φ of equation (6), the measurement Γ is thus obtained by

$$\Gamma(\xi, t) = \frac{c}{2A}\Phi(\mathbf{r}, t)|_{\mathbf{r}=\xi}. \quad (10)$$

In this paper we have used isotropic point sources located at a depth of $1/\mu_s$ below the surface, to model a collimated input beam incident normal on the surface. We have implemented the diffusion model ((6) and (9)) by using the finite element method. The domain Ω is divided into P elements, joined at D vertex nodes. The solution Φ of (6) is approximated by the piecewise linear function $\Phi^h(\mathbf{r}, t) = \sum_i^D \Phi_i(t)u_i(\mathbf{r}) \in \mathcal{U}^h$, where \mathcal{U}^h is a finite-dimensional subspace spanned by basis functions $u_j(\mathbf{r})$, $j = 1 \dots D$ chosen to have limited support. Likewise parameters μ_a and κ are expressed as piecewise linear functions in the nodal basis of the mesh. The problem of solving for Φ^h becomes one of sparse matrix inversion for which standard methods such as Cholesky decomposition or conjugate gradient solvers are readily available. The advantage of the FEM approach is its versatility which makes it applicable to complex geometries and highly inhomogeneous parameter distributions.

4. Inverse model

The forward model provides a map from parameter to data space, given by $y = F[\mu_a, \kappa]$. Given the vector of measurements, y^δ , we can define an objective function

$$\Psi = \frac{1}{2} \sum_{i=1}^s \sum_{j=1}^{m_i} \left(\frac{y_{ij}^\delta - F_{ij}[\mu_a, \kappa]}{\sigma_{ij}} \right)^2 \quad (11)$$

where σ_{ij} is an estimate of the standard deviation of measurement (ij) . The reconstruction then becomes a problem of minimization of Ψ by iteratively modifying solutions μ_a and κ . We employ a nonlinear conjugate gradient scheme together with a quadratic interpolation line search, which has been described (Arridge and Schweiger 1998), together with an efficient method to calculate the gradient of Ψ . Additional features of our reconstruction scheme include:

- (a) Prior information: for regularization we include additional energy functionals representing prior information. Following (Saqib *et al* 1997) we add Markov random field terms of the form

$$G(p) = \sum_{i=1}^D \sum_{j=1}^{nn(i)} h(p) |p_i - p_{n(i,j)}|^\alpha \quad (12)$$

to the objective function of equation (11), where p_i is the solution at node i , for p either μ_a or κ , $nn(i)$ is the number of neighbours of i , $n(i, j)$ is the j th neighbour of node i and $h(p)$ is a hyperparameter for p . The functional to be optimized is then $\tilde{\Psi} = \Psi + G(\mu_a) + G(\kappa)$. The derivative of $\tilde{\Psi}$ is added to the gradient of Ψ at each iteration of the optimization.

- (b) Solution filtering: in addition, after each iteration a filter can be applied to the reconstructed image, to approximate an embedding of the solution in a Sobolov space. We have implemented a median filter which has the effect of reducing noise whilst conserving edges. Note that for the reconstructions in section 6 no filter was applied.
- (c) Solution rescaling: for simultaneous (μ_a, κ) reconstructions, the μ_a and κ parts of the solution vector are scaled by the average values of their initial settings, $\bar{\mu}_a$ and $\bar{\kappa}$, during the initialization stage of the inverse solver, i.e. we work with $\tilde{\mu}_a = \mu_a / \bar{\mu}_a$ and $\tilde{\kappa} = \kappa / \bar{\kappa}$. This makes the solution entries dimensionless and ensures that the magnitudes of μ_a and κ entries are of comparable magnitude. The optimization is then performed in the scaled parameter space, to avoid the dominance of a single parameter.
- (d) Data rescaling: similarly, if more than one data set is used, each part of the data vector is scaled by the average value of the corresponding data set M in the measurement data vector, \bar{y}^M , to make sure that all measurement types contribute to the data norm to a comparable extent: $y^M \rightarrow \tilde{y}^M = y^M / \bar{y}^M$.
- (e) Choice of basis: while it is possible to employ the mesh used for forward calculations directly as a basis for the reconstructions, this is generally not appropriate since the resolution of the forward mesh is governed by considerations of numerical stability, and is normally considerably higher than the achievable image resolution. In the test reconstructions presented here we use a bilinear pixel grid of size 32×32 as the reconstruction basis, which reduces the dimensionality of the solution by approximately a factor of 4 compared to the forward mesh.

For the reconstructions presented below we used different FEM meshes for the calculation of simulated forward data, and for the forward model that implements the map $F[\mu_a, \kappa]$ within the inverse solver, to avoid the unrealistic cancellation of systematic errors (sometimes called an *inverse crime*). Gaussian-distributed random noise equivalent to 10^4 photons received at each detector is added to the data (Arridge *et al* 1995).

The image reconstruction package used for all reconstructions presented in this paper is TOAST (time-resolved optical absorption and scatter tomography), developed in our research group. A public domain version of this package for a limited number of UNIX platforms is available on the internet†.

5. Error surfaces for a single-perturbation case

Consider that the boundary $\partial\Omega$ is parametrized by θ . The data can be considered as a map $\Lambda(\theta_m, \theta_q)$ where θ_q indexes the source and θ_m indexes the measurement. Likewise the solution (in 2D) can be considered as two functions $\mu_a(x, y)$ and $\mu_s(x, y)$. A well known principle of inverse problems is that a single scalar mapping Λ of two variables cannot be used to reconstruct *two* functions of two variables (Isakov 1998). The proof of this result as applied to dc optical tomography was recently presented by Arridge and Lionheart (1998). Instead, either a complex mapping is required, in which case we require to recover functions in $\mathbb{R}^2 \times \mathbb{R}^2$ from a function in \mathbb{C}^2 , or we require more than one scalar mapping $\Lambda_1, \Lambda_2 \dots$. The latter is our approach.

To illustrate the reconstruction problem it would be helpful to visualize Ψ for data of a specific type as a function of the solution vectors μ_a and μ_s . In general this is not possible due to the high dimensionality of the solution space. However, to investigate the problem of simultaneous (μ_a, μ_s) reconstruction it may be sufficient to consider the simple problem of a single perturbation embedded in a homogeneous and known background. The solution vectors μ_a and μ_s then reduce to scalars $\mu_a^{(P)}$ and $\mu_s^{(P)}$ of the perturbation region. For this case we can explicitly plot Ψ as a function of $\mu_a^{(P)}$ and $\mu_s^{(P)}$

$$\Psi(\mu_a^{(P)}, \mu_s^{(P)}) = \frac{1}{2} \sum_{i=1}^s \sum_{j=1}^{m_i} \left(\frac{F_{ij}[\bar{\mu}_a^{(P)}, \bar{\mu}_s^{(P)}] - F_{ij}[\mu_a^{(P)}, \mu_s^{(P)}]}{\sigma_{ij}} \right)^2 \quad (13)$$

where $F_{ij}[\bar{\mu}_a^{(P)}, \bar{\mu}_s^{(P)}]$ is the reference data vector obtained for a specific set of perturbation values, $\bar{\mu}_a^{(P)}$ and $\bar{\mu}_s^{(P)}$. In all cases the background parameters $(\mu_a^{(B)}, \mu_s^{(B)})$ are kept fixed at the correct value.

We use a circular object of radius 25 mm with a homogeneous background of $\mu_a^{(B)} = 0.025 \text{ mm}^{-1}$ and $\mu_s^{(B)} = 2 \text{ mm}^{-1}$. Data are calculated at 16 equally spaced source positions and 16 detector positions, each placed between two sources. The reference data set is generated for perturbation parameters $\bar{\mu}_a^{(P)} = 0.05 \text{ mm}^{-1}$, $\bar{\mu}_s^{(P)} = 4 \text{ mm}^{-1}$, and test data are generated for all combinations of 41 $\mu_a^{(P)}$ values in the range from 0.025 mm^{-1} to 0.075 mm^{-1} , and 41 $\mu_s^{(P)}$ values in the range from 2 mm^{-1} to 6 mm^{-1} . Figure 1 shows the mesh geometry and location of the perturbation used for the data generation.

The graphs in figure 2 show the maps of $\Psi(\mu_a^{(P)}, \mu_s^{(P)})$ for the following data types: $\log E$, $\langle t \rangle$, $\langle t^2 \rangle$, c_2 , c_3 , $L(s = 0.001)$, $L(s = 0.01)$, $ML_1(s = 0.001)$, $ML_1(s = 0.01)$ and $ML_3(s = 0.001)$. Since the data are noiseless, all error maps reach their absolute minimum of zero at the correct perturbation data set of (0.05,4). However, to varying extent, characteristic for all types is an elongated 'valley' of low data error. In the presence of noise the position of the minimum of the data norm is likely to move far away from the true solution, if the gradient within these valleys is small, i.e. the effective null-space of the problem becomes large. Note that the orientation of the valley differs for different measurement types, which means that the relative sensitivity to changes in absorption and scatter varies between data types. Specifically, we note the following points:

† <http://www.medphys.ucl.ac.uk/toast/index.htm>

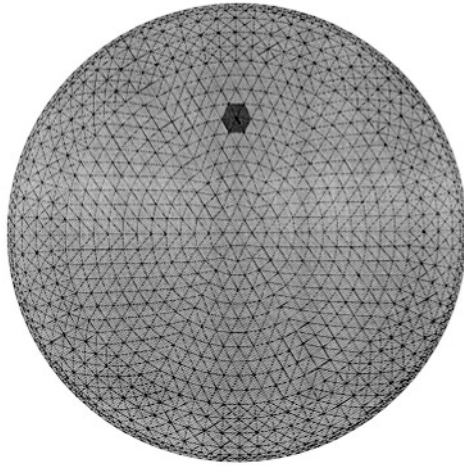


Figure 1. Mesh geometry and position of the perturbation used for error map data generation.

- (a) For $\log E$ data the form of the null space is approximately a reciprocal function of the form $\mu_a \mu_s = \text{const}$ so that any increase of one parameter can be compensated by a reduction of the other. This confirms the non-uniqueness result of dc data reported by Arridge and Lionheart (1998). It has been known that simultaneous reconstructions from $\log E$ of a pure absorption perturbation or a pure scatter perturbation always produce cross-talk artefacts (Arridge *et al* 1993b).
- (b) The error behaviour of $\log E$ and $\langle t \rangle$ is markedly different. This is in agreement with previous investigations on the effect of absorption and scattering perturbations on measurements, where we showed that absorbers and scatterers affect $\log E$ qualitatively in the same way, i.e. an increase in either causing a decrease in $\log E$, while they act qualitatively different on $\langle t \rangle$, such that $\langle t \rangle$ decreases with increasing μ_a , but increases with increasing μ_s (Schweiger *et al* 1992). Note that the latter condition is not generally true for the point-wise derivative, as $\partial \langle t \rangle_i / \partial \mu_s(\mathbf{r})$ can locally change sign.
- (c) For small s the error map of $L(s)$ is similar to that of $\langle t \rangle$. This follows directly from (4). With the approximation $e^{-st} \approx 1 - st$, L can be written as a linear function of $\langle t \rangle$:

$$L(s) \approx 1 - s \langle t \rangle. \quad (14)$$

- (d) On the other hand, for a high value of s the measurement error norm is more sensitive to errors in μ_s than μ_a . To understand this we look at the Laplace transform of (6)

$$\left(\frac{s}{c} + \mu_a - \nabla \cdot \kappa \nabla \right) L(\Phi(t), s) = L(q_0(t), s) \quad (15)$$

where we used $L(\partial \Phi / \partial t, s) = sL(\Phi, s)$. With substitution $L(\Phi(t), s) \rightarrow \Phi'$, $L(q_0(t), s) \rightarrow q'_0$ we obtain the time-independent diffusion equation with the modified absorption parameter $\mu'_a = s/c + \mu_a$. Since the measurement perturbation is essentially proportional to the logarithm of the parameter perturbation (Schweiger *et al* 1992), a large s reduces the influence of μ_a .

- (e) Conversely the error norm of central moments is more sensitive to errors in μ_a than μ_s .
- (f) For Mellin–Laplace data, an increase in s emphasizes the μ_s sensitivity, while the use of a higher moment in t increases the sensitivity to μ_a .

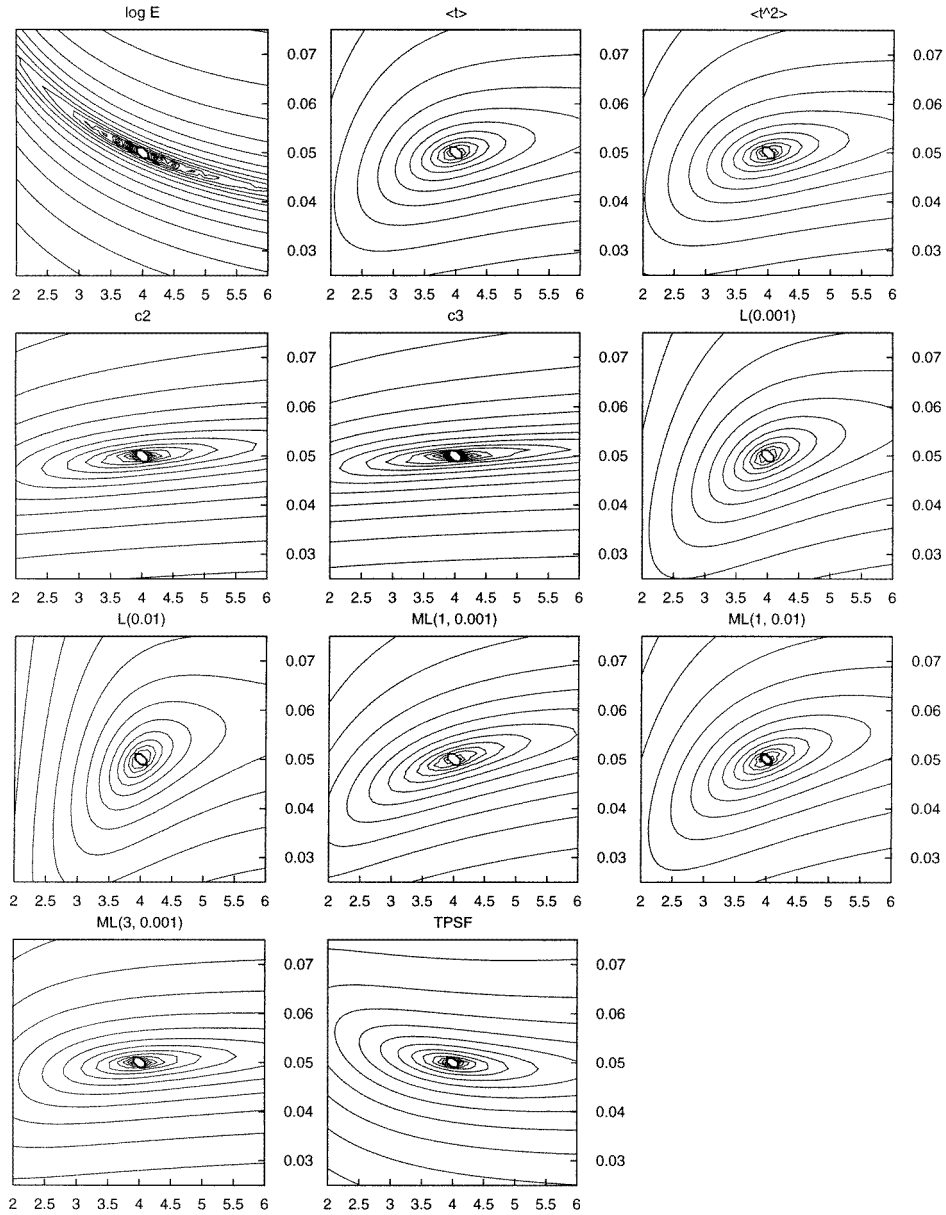


Figure 2. Objective functions for single-perturbation case as a function of the scattering coefficient (abscissa) and absorption coefficient (ordinate) of the perturbation. The absolute minimum of the function is in the centre of each plot, at the reference parameters of the perturbation of $\mu_a = 0.05 \text{ mm}^{-1}$ and $\mu_s = 4 \text{ mm}^{-1}$. Background values are $\mu_a = 0.025 \text{ mm}^{-1}$ and $\mu_s = 2 \text{ mm}^{-1}$.

Figure 2 also shows the error surface for the full temporal profile (TPSF), $\Gamma(t_i)$, sampled at discrete time steps t_i . In this case the error norm is defined as the RMS difference of the reference and the perturbation profile at all time samples. It exhibits a more clearly defined minimum, than $\log E$, indicating that full Γ data provide a better means to separate μ_a and μ_s .

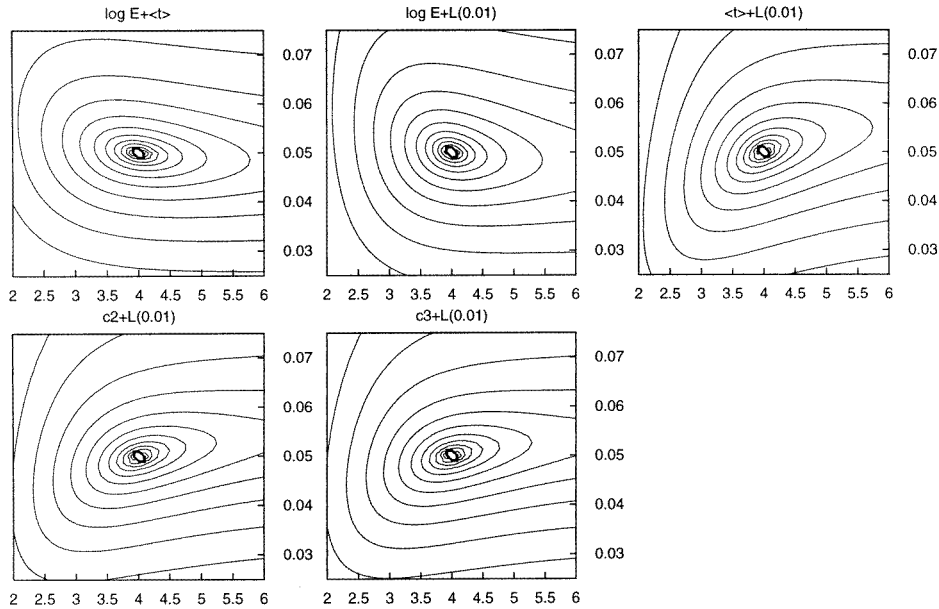


Figure 3. Objective functions for combinations of data types.

than $\log E$. Note, however, that calculation of Γ is computationally expensive and normally not suitable for reconstruction.

Error map distributions like that of $\log E$ indicate an ambiguity between absorption and scatter solutions that cannot be resolved by the inverse scheme. One has to adopt parameter types which exhibit a more well-defined minimum, such as $\langle t \rangle$. Furthermore one can aim to improve reconstruction stability and convergence rate by combining several suitable data types (Arridge and Schweiger 1993).

Alternatively, it is possible to employ an alternating scheme, where the reconstruction program switches between reconstruction of μ_a from one data type, and μ_s from another. By selecting data types which are primarily sensitive to only one parameter, the artefacts introduced by errors in the estimate of the other parameter are minimized. Under this aspect, we conclude from the error maps in figure 2 that the skew (c_3) is a good choice for the reconstruction of μ_a , as its error norm varies with μ_a significantly more than with μ_s , while conversely $L(s = 0.01)$ is suitable for the reconstruction of μ_s .

For the simultaneous reconstruction we require a combination of measurement types for which the sums of the error norms exhibit a clearly defined minimum, to avoid the μ_a/μ_s ambiguity of the single-measure case. The graphs of figure 3 show error maps for various combinations of measurement types. It appears that in some cases the problem is better posed than for single type reconstructions, e.g. for the combination $\log E + L(0.01)$. For other combinations the improvement is not quite as obvious, but in the reconstructions below we will restrict the reconstructions from multiple data to normalized data types, due to their greater robustness against data errors, and include reconstructions from $\log E$ only for the purpose of comparison.

Finally we would like to note that the application of the Laplace transform to Γ simulates time-gating techniques by suppressing late-arriving photons. Increasing s will therefore eventually lead to similar problems of poor photon statistics as seen in explicit time-gating during data acquisition. This imposes an upper limit to the value of s , both with respect to the

signal-to-noise ratio of the data, and the numerical stability of the forward solver. In the FEM forward model, a high s value has to be matched with a sufficiently highly resolved mesh to guarantee the numerical stability of the calculation. For the circular object used here a typical mesh size of the order of 3000 elements was used to generate all data except $L(s = 0.01)$, which required a mesh with about twice the number of elements.

Although the emphasis of this paper is on time-domain data types, single-perturbation error maps can equally be generated for data types provided by frequency-domain imaging systems. In the frequency domain, the measured quantity is the complex exitance (\hat{E}), given a harmonic input signal. In practice, frequency domain data acquisition systems usually measure the phaseshift ($\arg \hat{E}$) and modulation depth ($\text{mod} \hat{E}$) of the response signal. In figure 4 we show error maps for \hat{E} , its real ($\text{Re} \hat{E}$) and imaginary parts ($\text{Im} \hat{E}$), as well as $\arg \hat{E}$ and $\text{mod} \hat{E}$ at three different source modulation frequencies of 10, 100 and 500 MHz. Most frequency-domain data error maps exhibit an elongated feature around the minimum similar to the time-domain cases. The only data type with a clearly defined minimum is the phaseshift ($\arg \hat{E}$). There is only a moderate dependency of the shape of the error map on modulation frequency. The only significant effect is a change in the orientation of the valley for $\text{Im} \hat{E}$ (500 MHz).

6. Reconstruction results

To test the reconstruction performance predictions of the previous chapter for different measurement types we carried out two-dimensional test reconstructions from simulated data of a circular test object with embedded circular and elliptic inhomogeneities which differ in both absorption and scatter coefficient from the background. Forward data of boundary measurements are generated with the finite element forward model, assuming that each measurement is composed of a fixed number of 10^4 received photons. In practice this would be achieved by adapting the source power or integration time corresponding to the attenuation for each source/detector pair. The distribution of absorption and scatter parameters is shown in figure 5. The values of the optical parameters of the background (region 0) and embedded objects (regions 1–7) are listed in table 1, and the geometric properties of internal regions in table 2. The refractive index of the surrounding medium is set to 1 (air).

Table 1. Optical parameters of circular test object.

Region	μ_a (mm ⁻¹)	μ_s (mm ⁻¹)	ν
0	0.025	2	1.4
1	0.05	2	1.4
2	0.05	1	1.4
3	0.0125	4	1.4
4	0.0167	3	1.4
5	0.0375	1.33	1.4
6	0.025	4	1.4
7	0.05	2	1.4

For the forward data generation the object is discretized into a mesh of triangular elements (3730 nodes, 7261 elements). The internal structure of the object is taken into account by an adaptive meshing algorithm to ensure accurate modelling of the inhomogeneities (Peraire *et al* 1987). The mesh structure is shown in figure 6. 32 sources and 32 detectors are placed equally spaced along the boundary. For each source, data at 30 detector locations are computed, leaving out the two detectors adjacent to the source in each case. This reduces the occurrence of boundary artefacts in the reconstructions and also makes sure that the distance between

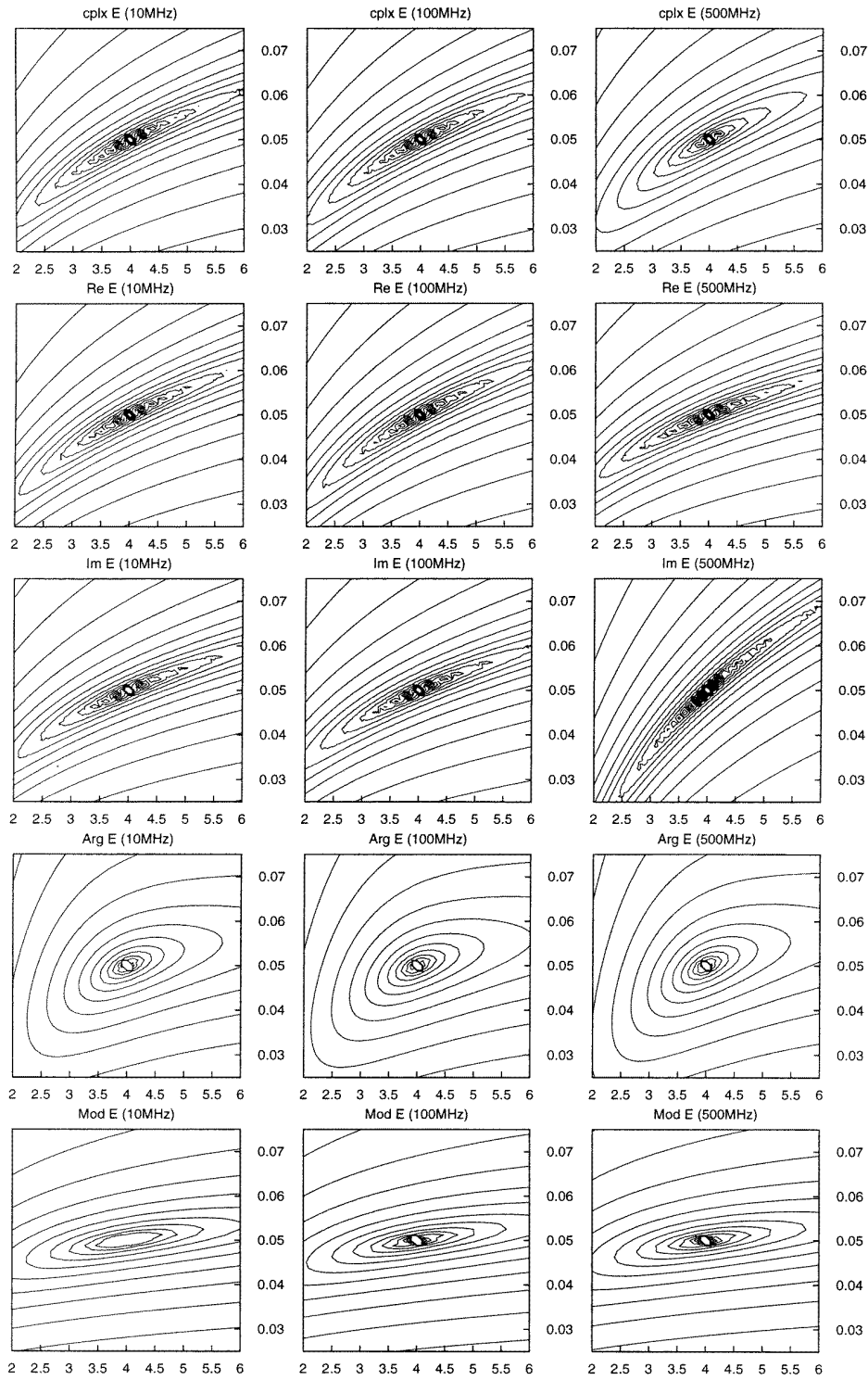


Figure 4. Objective functions for frequency-domain measurement types at different modulation frequencies.

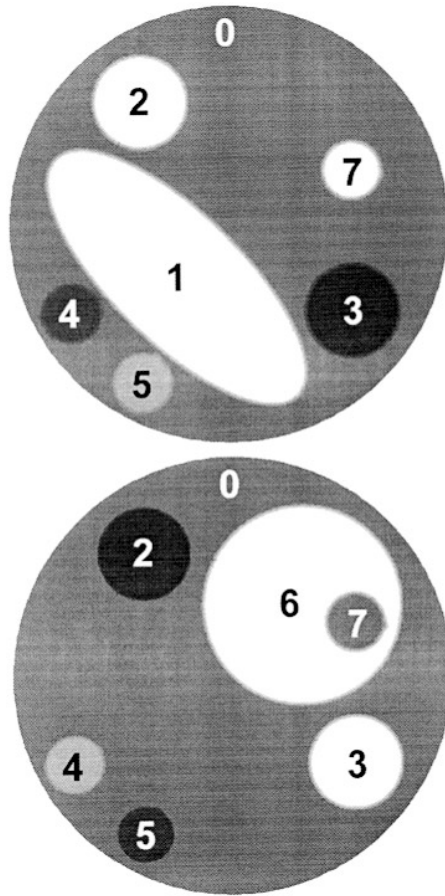


Figure 5. Circular test case: target images of absorption (top) and scatter coefficient (bottom). For optical properties of background (region 0) and embedded objects (regions 1–7) see table 1.

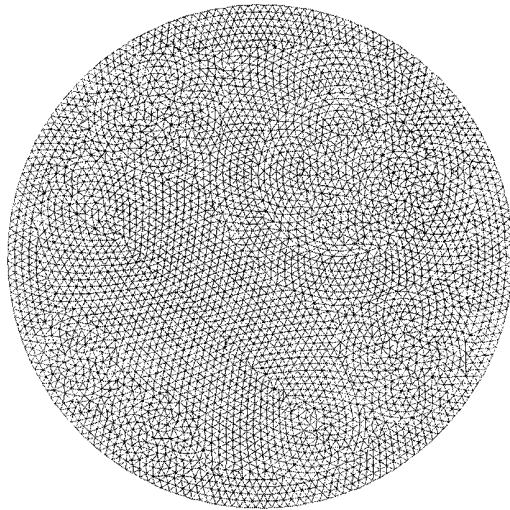
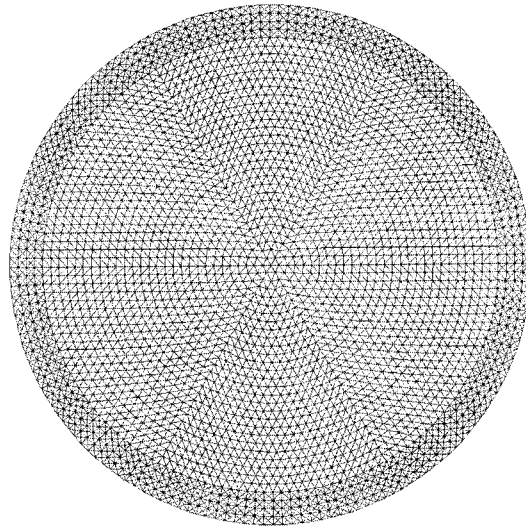


Figure 6. Mesh used by the forward model. The internal structure of the embedded inhomogeneities is used in the adaptive meshing process.

Table 2. Geometric specification of the internal structure of the test object.

Region	Outline description
0 (outer boundary)	Circle: centre (0,0), radius 25
1	Ellipse: centre (-6, -6), semi-major axis 19, Semi-minor axis 7, rotation 45°
2	Circle: centre (-10, 14), radius 5
3	Circle: centre (14, -10), radius 5
4	Circle: centre (-18, -10), radius 3
5	Circle: centre (-10, -18), radius 3
6	Circle: centre (8, 8), radius 11
7	Circle: centre (14, 6), radius 3

**Figure 7.** Mesh used by the inverse model. No internal structural information is used.

sources and detectors is sufficiently large in all cases for the diffusion forward model to be applied (Kienle and Patterson 1997).

The reconstruction uses a mesh with identical outer boundary, but without using any information about internal boundaries between regions of different parameters (see figure 7). The initial guess for the reconstruction in each case is a homogeneous distribution of $\mu_a = 0.025 \text{ mm}^{-1}$ and $\mu_s = 2 \text{ mm}^{-1}$. We use the background parameters as a starting point to avoid additional convergence problems which would obscure the effect of the data types which we want to emphasize in this paper. Reconstructions are terminated after 50 iterations. As the reconstruction basis we used a regular 32×32 pixel grid. For reference, the target images expressed in this basis are shown in figure 8.

The regularization parameters h and α of equation (12) were obtained heuristically, but the same parameters were used for all cases to allow a fair comparison. We use $\alpha = 1.1$, $h(\mu_a) = 10^{-6}$ and $h(\kappa) = 10^{-4}$. A detailed study of the choice of hyperparameters is required, but this is beyond the scope of this paper. For a discussion of Markov random fields and Gibbs distributions in image reconstruction see, for example, Geman and Geman (1984).

Reconstructions were performed on a Pentium II-450 with 1 GB of RAM. Computation times varied between 10 and 90 s per iteration, depending on the data types used.

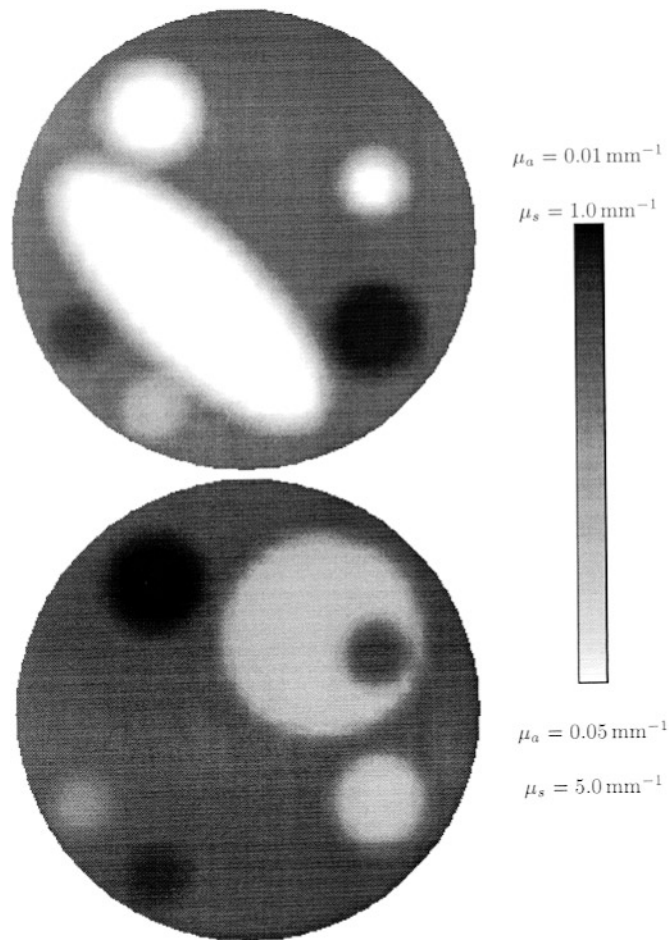


Figure 8. Reference target images of absorption and scatter, expressed in the 32×32 pixel basis of the inverse solution.

Figures 9 and 10 show reconstructed images of μ_a (left column) and μ_s (right column) after 50 conjugate gradient iterations obtained from the following different data types, as follows: figure 9, from top to bottom: $\log E$, $\langle t \rangle$ and c_3 ; figure 10, from top to bottom: $L(0.001)$, $ML_1(0.01) + ML_3(0.001)$ and $c_3 + L(0.001)$. All reconstructed images are scaled to a common range ($0.01 \text{ mm}^{-1} \leq \mu_a \leq 0.05 \text{ mm}^{-1}$ for μ_a images, and $1 \text{ mm}^{-1} \leq \mu_s \leq 5 \text{ mm}^{-1}$ for μ_s images).

The results can be summarized in the following points:

- (a) Reconstruction from $\log E$ recovers only the largest objects (regions 1 and 6), at very low contrast, and, more importantly, cannot distinguish between absorption and scatter features. The μ_a and μ_s images look essentially the same in this case, with region 1 appearing in the μ_s image and region 6 appearing in the μ_a image.
- (b) Reconstruction from $\langle t \rangle$ does provide separation of absorption and scatter features, but also produces significant artefact, especially in the absorption image, along the boundary.

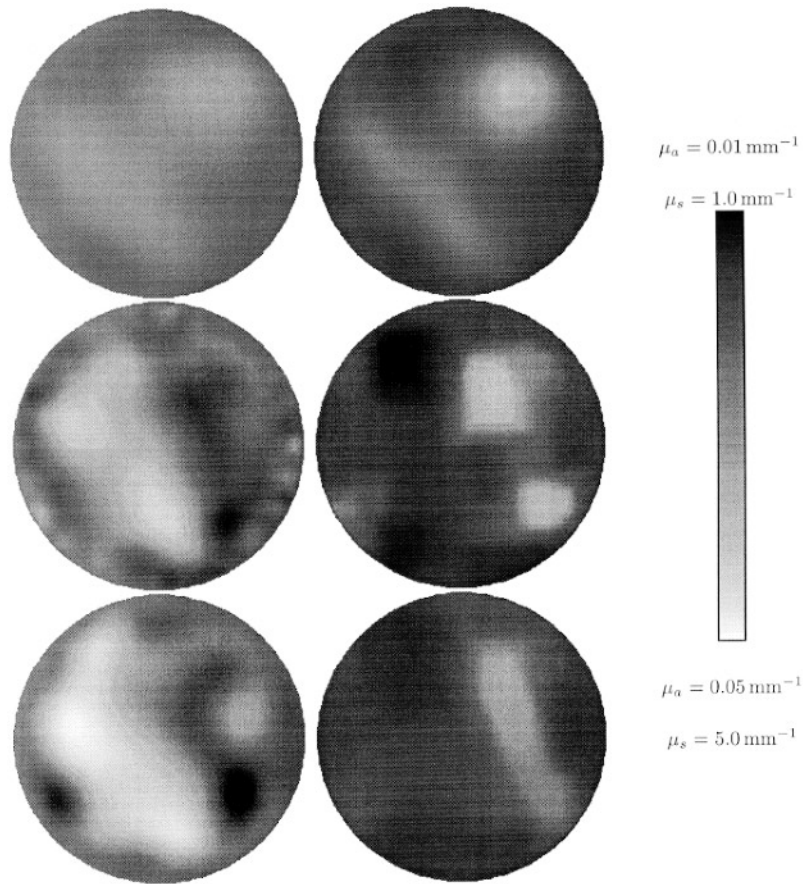


Figure 9. Reconstruction from different data types. Left column, μ_a ; right column, μ_s . Rows from top to bottom: reconstruction from $\log E$, from $\langle t \rangle$, and from c_3 .

- (c) Reconstruction from c_3 yields a good μ_a image with higher contrast than the $\langle t \rangle$ image, and also begins to recover the embedded absorption region (7), but the μ_s image is poor. The good quality of the absorption image is consistent with the shape of the error map, which predicts a high sensitivity of c_3 to absorption, with little influence from the scatter distribution (figure 2).
- (d) Conversely, reconstruction from $L(0.001)$ yields a good μ_s image with all scatter objects clearly defined, but the μ_a image has low resolution and contrast. Again this behaviour corresponds with the error map which is predominantly sensitive to scatter changes.
- (e) The reconstruction from two Mellin–Laplace data sets ($ML_1(0.01) + ML_3(0.001)$) also achieves a good separation between absorption and scatter features. It produces similar results to the mean time reconstruction, with a well-defined scatter image, but relatively low resolution and boundary artefacts in the absorption image.
- (f) The reconstruction from a combination of c_3 and $L(0.001)$ gives the best results for both μ_a and μ_s reconstruction, where objects are well-defined with little cross-talk between the images. The large μ_s region (6) and its embedded low-scatter/high-absorption region are recovered with good resolution. Quantitative recovery of perturbation values is superior to the other reconstructions.

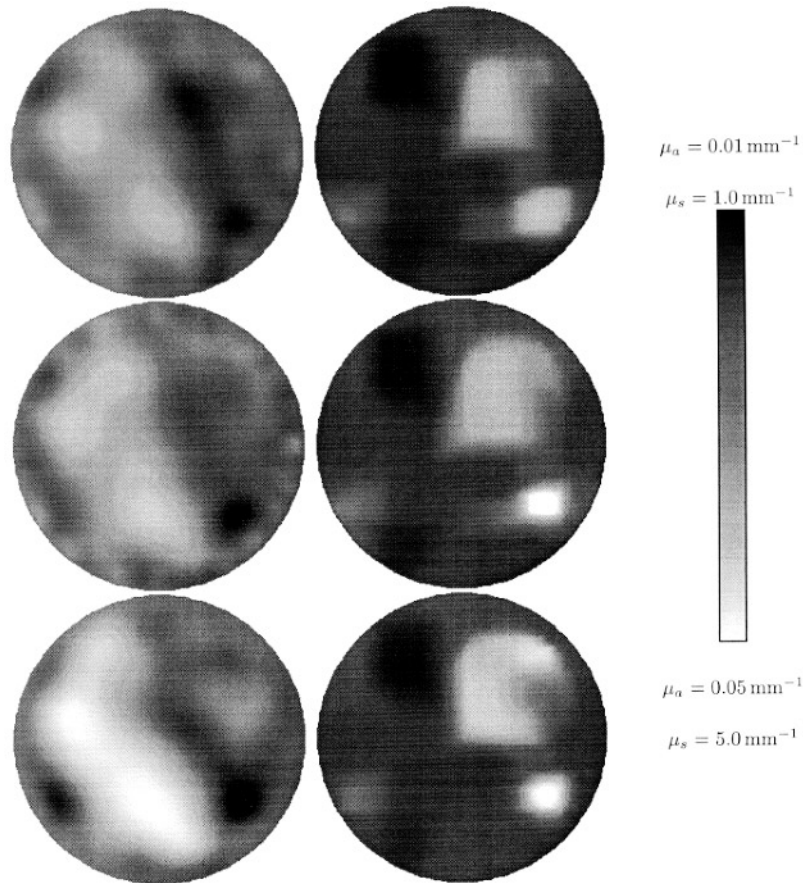


Figure 10. Reconstruction from different data types. Left column, μ_a ; right column, μ_s . Rows from top to bottom: reconstruction from $L(0.001)$, from $ML_1(0.01) + ML_3(0.001)$ and from $c_3 + L(0.001)$.

Figure 11 shows the L_2 norms ($A_i^{-1} \int_{\Omega_i} \|x(r) - \bar{x}(r)\|^2 dr$, $x \in \{\mu_a, \mu_s\}$) of the solutions $x(r)$, separated in the eight regions Ω_i of the test object, against target values $\bar{x}(r)$ and normalized by region areas A_i , for all reconstructions from the data types discussed above. These solution norms provide some quantitative indication as to the reconstruction performance and ability to recover absolute perturbation values.

The graphs confirm the results outlined above: Reconstructions from $\log E$ yield poor quantitative results, while other measurement types, in particular the $c_3 + L(0.001)$ combination, achieve better absolute values. Certain regions such as the embedded low-scatter/high-absorption region 7 appear to pose particular difficulties to the reconstruction, where all data types provide poor quantitation.

7. Conclusion

We have discussed the reconstruction problem in OT with emphasis on the simultaneous reconstruction of absorption and scattering. Simultaneous reconstruction is required where both parameter types are unknown, even if only one of them is of interest, because an error

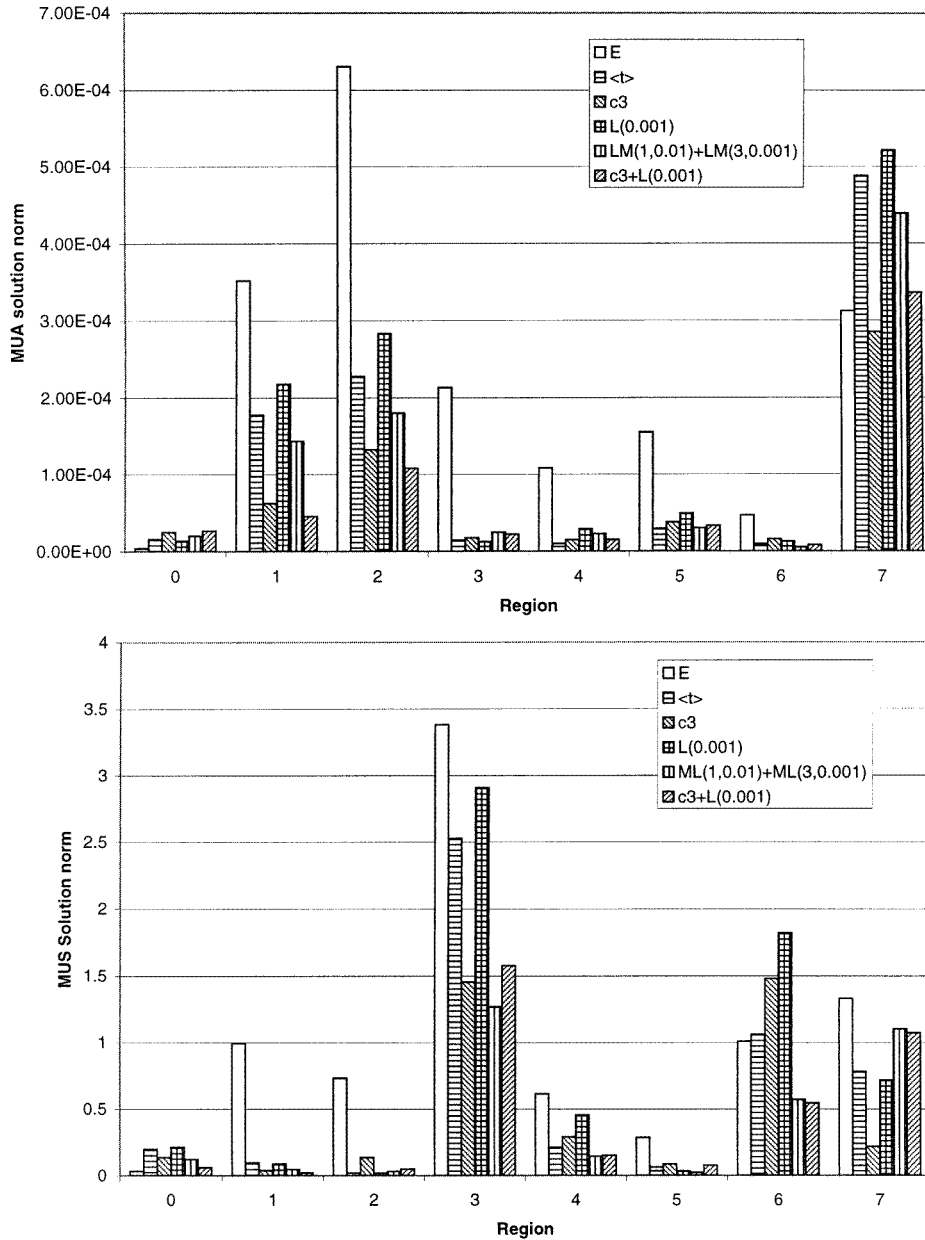


Figure 11. Solution error norms for each parameter region of the test object. Top, error norms for absorption images; bottom, norms for scatter images.

in one parameter will manifest itself as an artefact in the other. We have presented a range of data types that can be derived from the temporal profile of a time-domain imaging system, and demonstrated that the relative measurement sensitivity to perturbations in the absorption and scatter distribution of the transilluminated object depends on the type of data used. Certain data types, in particular dc data of steady-state attenuation, are unsuitable to reconstruct absorption and scatter simultaneously, because they exhibit no well-defined minimum of the objective

function in the (μ_a, κ) parameter space. Other data types are predominantly sensitive to a single-parameter, for example central moments (c_n) pick up mainly perturbations in absorption, but are insensitive to scatter. This feature might be used in single-parameter reconstructions, to minimize artefacts caused by cross-talk.

We find that to suppress cross-talk artefact in simultaneous reconstructions, and to obtain satisfactory results with good contrast and resolution in both images, the use of multiple data types is required. A combination of skew and Laplace transform of the temporal profile proved to provide the best images among the data types investigated here. These data types are orthogonal in the sense that each is predominantly sensitive to a single parameter, so that their combination provides a set of largely independent data which maximizes the information content required to separate the μ_a and μ_s images.

Acknowledgment

This work was supported by the Wellcome Trust.

Appendix

To allow the direct comparison of our reconstructions with algorithms developed by other groups, we propose the test object used in this paper as a standard problem against which to test reconstruction algorithms. We include the geometric information of the internal structure in table 2, to enable other researchers to regenerate forward data and apply their imaging methods to them. The optical properties of the regions are listed in table 1. In the future we propose to generate a physical test phantom with the same structure and optical properties, and to make measurements obtained from it publicly available as a reference data set.

References

- Arridge S R and Hebden J C 1997 Optical imaging in medicine: II. Modelling and reconstruction *Phys. Med. Biol.* **42** 841–53
- Arridge S R, Hiraoka M and Schweiger M 1995 Statistical basis for the determination of optical pathlength in tissue *Phys. Med. Biol.* **40** 1539–58
- Arridge S R and Lionheart W R B 1998 Non-uniqueness in diffusion-based optical tomography *Opt. Lett.* **23** 882–4
- Arridge S R and Schweiger M 1993 The use of multiple data types in time-resolved optical absorption and scattering tomography (TOAST) *Proc. SPIE* **2035** 218–29
- 1995a Sensitivity to prior knowledge in optical tomographic reconstruction *Proc. SPIE* **2389** 378–88
- 1995b Direct calculation of the moments of the distribution of photon time of flight in tissue with a finite-element method *Appl. Opt.* **34** 2683–7
- 1998 A gradient-based optimisation scheme for optical tomography *Opt. Express* **2** 213–26 (<http://www.epubs.osa.org/oearchive/source/4014.htm>)
- Arridge S R, Schweiger M and Delpy D T 1992 Iterative reconstruction of near-infrared absorption images *Proc. SPIE* **1767** 372–83
- Arridge S R, Schweiger M, Hiraoka M and Delpy D T 1993a A finite element approach for modeling photon transport in tissue *Med. Phys.* **20** 299–309
- 1993b Performance of an iterative reconstruction algorithm for near infrared absorption and scatter imaging *Proc. SPIE* **1888** 360–71
- Bronnikov A V 1995 Approximate reconstruction of attenuation map in SPECT imaging 1995 *IEEE Trans. Nucl. Sci.* **42** 1483–8
- Cai W, Das B B, Liu F, Zevallos M, Lax M and Alfano R R 1996 Time resolved optical diffusion tomographic image reconstruction in highly scattering turbid media *Proc. Natl Acad. Sci. USA* **93** 13 561–4
- Censor Y, Gustafson D E, Lent A and Tuy H 1979 A new approach on the emission computerized tomography problem: simultaneous calculation of attenuation and activity coefficients *IEEE Trans. Nucl. Sci.* **26** 2775–9

- Chance B, Maris M, Sorge J and Zhang M Z 1990 A phase modulation system for dual wavelength difference spectroscopy of haemoglobin deoxygenation in tissue *Proc. SPIE* **1204** 481–91
- Colak S B, Hooft G W, Papaioannou D G and van der Mark M B 1996 3D backprojection tomography for medical optical imaging *OSA Trends in Optics and Photonics on Advances in Optical Imaging and Photon Migration* ed R R Alfano and J G Fujimoto (Washington, DC: Optical Society of America) pp 294–8
- Delpy D T, Cope M, van der Zee P, Arridge S R, Wray S and Wyatt J 1988 Estimation of optical pathlength through tissue from direct time of flight measurement *Phys. Med. Biol.* **33** 1433–42
- Edwards A D, Wyatt J S, Richardson C E, Delpy D T, Cope M and Reynolds E O R 1988 Cotside measurement of cerebral blood flow in ill newborn infants by near infrared spectroscopy *Lancet* **ii** 770–1
- Farrell T J and Patterson M S 1992 A diffusion theory model of spatially resolved, steady-state diffuse reflectance for the noninvasive determination of tissue optical properties *in vivo Med. Phys.* **19** 879–88
- Fishkin J B and Gratton E 1993 Propagation of photon-density waves in strongly scattering media containing an absorbing semi-infinite plane bounded by a straight edge *J. Opt. Soc. Am. A* **10** 127–40
- Geman S and Geman D 1984 Stochastic relaxation, Gibbs distributions, and the Bayesian restoration of images *IEEE Trans. Pattern Anal.* **6** 721–41
- Hebden J C, Arridge S R and Delpy D T 1997 Optical imaging in medicine: I. Experimental techniques *Phys. Med. Biol.* **42** 825–40
- Hebden J C, Kruger R A and Wong K S 1991 Time resolved imaging through a highly scattering medium *Appl. Opt.* **30** 788–94
- Isakov V 1998 *Inverse Problems in Partial Differential Equations* (New York: Springer)
- Jiang H, Paulsen K D and Osterberg U L 1995 Optical image reconstruction using frequency-domain data: simulations and experiments *J. Opt. Soc. Am. A* **13** 253–66
- Jiang H, Paulsen K D and Österberg U L 1996 Optical image reconstruction using dc data: simulations and experiments *Phys. Med. Biol.* **41** 1483–98
- Jiang H, Paulsen K D, Österberg U L and Patterson M S 1998 Frequency-domain near-infrared photo diffusion imaging: initial evaluation in multitarget tissue-like phantoms *Med. Phys.* **25** 183–93
- Kienle A and Patterson M S 1997 Improved solutions of the steady-state and the time-resolved diffusion equations for reflectance from a semi-infinite turbid medium *J. Opt. Soc. Am. A* **14** 246–54
- Madsen S J, Patterson M S, Wilson B C, Jaywant S M and Othonos A 1993 Numerical modelling and experimental studies of light pulse propagation in inhomogeneous random media *Proc. SPIE* **1888** 90–102
- Ntziachristos V, Ma X, Yodh A G and Chance B 1999 Multichannel photon counting instrument for spatially resolved near infrared spectroscopy *Rev. Sci. Instrum.* **70** 193–201
- O’Leary M A, Boas D A, Chance B and Yodh A G 1995 Experimental images of heterogeneous turbid media by frequency-domain diffusing-photon tomography *Opt. Lett.* **20** 426–8
- Peraire J, Vahdati M, Morgan K and Zienkiewicz O C 1987 Adaptive remeshing for compressible flow computations *J. Comput. Phys.* **72** 449–66
- Pogue B W, Patterson M S, Jiang H and Paulsen K D 1995 Initial assessment of a simple system for frequency domain diffuse optical tomography *Phys. Med. Biol.* **40** 1709–29
- Saquist S S, Hanson K M and Cunningham G S 1997 Model-based image reconstruction from time-resolved diffusion data *Proc. SPIE* **3034** 369–80
- Schweiger M and Arridge S R 1997 The finite element method for the propagation of light in scattering media: frequency domain case *Med. Phys.* **24** 895–902
- 1998 Comparison of 2D and 3D reconstruction methods in optical tomography *Appl. Opt.* **37** 7419–28
- Schweiger M, Arridge S R and Delpy D T 1993 Application of the finite-element method for the forward and inverse models in optical tomography *J. Math. Imag. Vision* **3** 263–83
- Schweiger M, Arridge S R, Hiraoka M and Delpy D T 1992 Application of the finite element method for the forward model in infrared absorption imaging *Proc. SPIE* **1768** 97–108
- 1995 The finite element model for the propagation of light in scattering media: boundary and source conditions *Med. Phys.* **22** 1779–92
- Walker S A, Fantini S and Gratton E 1996 Back-projection reconstructions of cylindrical inhomogeneities from frequency domain optical measurements in turbid media *OSA Trends in Optics and Photonics on Advances in Optical Imaging and Photon Migration* ed R R Alfano and J G Fujimoto (Washington, DC: Optical Society of America) pp 137–41
- Wyatt J S, Cope M, Delpy D T, Richardson C E, Edwards A D, Wray S C and Reynolds E O R 1990 Quantitation of cerebral blood volume in newborn infants by near infrared spectroscopy *J. Appl. Phys.* **68** 1086–91